Compatibility of Wrought Superalloys with Supercritical CO_2

B. A. Pint
Oak Ridge National Laboratory, P.O. Box 2008, Oak Ridge, TN 37831-6156 USA
(pintba@ornl.gov, 865-576-2897)

ABSTRACT

Supercritical CO_2 (sCO_2) power cycles, particularly direct-fired cycles, have the possibility of revolutionizing clean fossil energy with peak temperatures above 700°C and wrought precipitation strengthened alloys like Haynes 282™ for structural components. At temperatures <650°C, it would be desirable to use less expensive alloys, however, steels are known to be susceptible to carburization. Laboratory 300 bar sCO_2 autoclave results were collected on a range of alloys including less expensive Ni-based alloys like 825 compared to advanced austenitic steels like alloy 709 at 600°C. Both alloys 825 and 709 formed thin, protective Cr-rich oxides after 1,000 h. Alloy 825 also was exposed for 1,000 h in sCO_2 at 800°C and compared to a range of Ni-based alloys. Comparing alloys 625, 825 and 282, the mass gain increased with increasing alloy Ti content under these conditions. High Al superalloys did not perform significantly better under these conditions at 800°C.

Keywords: supercritical carbon dioxide, environmental resistance

INTRODUCTION

Supercritical CO_2 (sCO_2) is a potential working fluid for a number of power generation technologies including fossil, nuclear, geothermal, concentrating solar power (CSP) and waste heat recovery [1-4]. The supercritical state offers a unique set of properties and CO_2 has a relatively low critical point (31°C/73.8 bar). Nickel-based alloys have been found to be very compatible with sCO_2 at 700°-800°C [5-13], where greater than 50% cycle efficiency is predicted [14]. Considerable development work was completed by the Advanced Ultra-supercritical (A-USC) consortium which had a goal of increasing steam temperatures to 760°C/34.5 MPa (1400°F/5000 psi) in fossil-fired boilers [15]. The accomplishments included qualifying precipitate-strengthened (PS) γ/γ′ alloys 740 (and 740H) and 282 [16,17] into the ASME boiler and pressure vessel code. Their high strength reduces the required wall thickness on pipes and tubes compared to conventional solid solution strengthened (SS) alloys (e.g., 625, 230, 617) [11].

However, for sCO_2-based power cycles to be commercially competitive, lower cost materials are needed in the lower temperature components in the cycle. There is concern about the use of steels in sCO_2 because of prior experience with Grade 9 (Fe-9wt.%Cr-1Mo) in the UK advanced gas cooled reactors (AGRs) operated with 42 bar CO_2 (sub-critical conditions) at ≤550°C where severe internal carburization was observed [18]. A review concluded that creep-strength enhanced ferritic (CSEF) 9-12%Cr steels were limited to 450°C in sCO_2 [19], significantly lower than the 580°-600°C limit in supercritical steam [20]. A nuclear fuel cladding study found that a stainless steel such as type 316FR had much better oxidation resistance than 9-12%Cr CSEF steels in sCO_2 but 316FR began to show accelerated oxidation at 600°C [21]. Carbon ingress in Fe-based alloys exposed to CO_2 environments has been observed for many years

[22-24] but more recent studies by Young and co-workers [25,26] has clearly explained the thermodynamic driving force for this behavior.

The current work is focused on identifying lower cost alloys for sCO_2 cycle components, particularly in the transition region where steels may not be sufficiently compatible with sCO_2. The current comparison included the high-Fe content, lower cost, alloy 825 and conventional and advanced austenitic steels at 600°C. Alloy 825 also was exposed at 800°C and compared to Ni-based PS and superalloys and one Co-based alloy that may be candidates for sCO_2 turbine components.

EXPERIMENTAL PROCEDURE

The chemical compositions of the structural alloys studied are shown in Table 1. Alloy coupons (~12 x 20 x 1.5mm) were polished to a 600 grit finish and ultrasonically cleaned in acetone and methanol prior to exposure. The specimens were exposed for 500-h cycles at 600° and 800°C in 300 bar research grade (RG) sCO_2. Previously, the H_2O content of the RG CO_2 was measured by the vendor in 6 cylinders as 4.1±0.7 ppm and the O_2 content is reported as <5ppm [13]. The exposures were conducted in a vertically oriented autoclave (~266 mm x 83 mm inner diameter) made from alloy 282 and operated inside a three-zone furnace with an alloy 282 sample rack that sat on the bottom of the autoclave. The fluid flow rate was ~2 ml/min and additional details of the system have been provided elsewhere [6,9,12,13]. The specimens were heated to temperature over several hours (~2°C/min) in sCO_2, held at temperature ±2°C and cooled in CO_2 to room temperature after exposure.

Because of variability observed in previous experiments, 4-6 coupons of each alloy were exposed in each condition with one specimen removed after 500 h. Before and after exposure, all specimens were weighed using a Mettler Toledo model XP205 balance with an accuracy of ~±0.04 mg or 0.01 mg/cm^2. For characterization, specimens were Cu-plated before being sectioned and mounted for light microscopy and scanning electron microscopy (Tescan model MIRA3) equipped with energy dispersive X-ray spectroscopy (EDS).

RESULTS

Figure 1 shows the mass change data for specimens exposed to 300 bar RG sCO_2 for 500 and 1000 h at 600°C. The conventional 316H austenitic steel specimens showed high mass gains under these conditions. Table 1 shows that it has the lowest combination of Cr and Ni and it will not be further discussed here. Specimens of cast CF8C-Plus and wrought 253MA showed considerably lower mass gains under these conditions. This is an expected benefit of higher Cr and Ni contents in these alloys, Table 1. However, the mass gains were much higher than the 709 and 825 specimens, Figure 1.

Figure 2 shows polished cross-sections of one of the specimens after 1000 h sCO_2 exposures at 600°C. The 253MA and CF8C-Plus specimens showed more significant nodule formation than the 709 and 825 specimens, consistent with the mass change. Characterization using EDS revealed that the nodules were Fe-rich with the typical duplex structure of inward growing Cr-rich spinel-type oxide and outward growing Fe-rich oxide. The higher Ni and Cr contents in these alloys may prevent the nodules from growing and spreading to form a continuous duplex structure, like that formed on 316H in sCO_2 at 650°C [27]. However, longer exposures are needed to determine to what extent the nodules will continue to grow. Perhaps of more importance is the C ingress that may have occurred during exposure. Those measurements by bulk combustion analysis and surface measurements by sputtering glow discharge optical emission spectroscopy (GDOES) or electron-probe microanalysis (EPMA) using wavelength dispersive spectroscopy are in progress.

Figures 2c and 2d show the thin reaction products formed on 709 and 825 specimens, respectively. Because the Cu plating separates at the scale interface, the scale on the 709 substrate looks thicker in Figure 2c. Higher resolution SEM imaging was needed to characterize the scale. A few small oxide nodules also were observed on these specimens. Figure 3a shows a SEM image of the thin scale formed on alloy 709 at

600°C. The associated EDS maps in Figure 3 show that the oxide scale is enriched in Cr, Mn and a small amount of Si. The Cr map in Figure 3b shows Cr depletion near the metal-scale interface but the ~1μm spatial resolution of EDS makes it difficult to quantify the depletion which appears to be on the order of 1μm in depth. Figure 4 shows a similar SEM/EDS analysis of one 825 specimen exposed for 1000 h at 600°C. In this case, the Cr-rich oxide appears to contain Ti and Mn with some Mo-rich precipitates evident. Figure 4b also shows a small amount of Cr depletion near the metal-scale interface that was measured as 15 wt.% (compared to 22.7%Cr measured in the bulk alloy, Table 1).

Figure 5 shows mass change measurements after 500 and 1000 h at 800°C in 300 bar RG sCO_2. Despite the high Fe content (30.8%) in alloy 825, the average mass gains for this Cr_2O_3-forming alloy were similar to those for 282 and slightly higher than the specimens of alloy 617 and Co-based alloy 188. Figure 6a shows example cross-sections of the scales formed after 1000 h at 800°C in sCO_2. The external scale formed on 825 (Figure 6b) was slightly thicker than that formed on 282 (Figure 6a) but with less internal oxidation. Additional characterization of the Cr_2O_3-forming alloys is in progress. A glow discharge optical emission spectroscopy (GDOES) sputter depth profile of the 825 specimen exposed for 1000 h at 800°C in sCO_2 showed no evidence of C ingress, similar to other Ni-based alloys exposed for up to 10,000 h at 750°C in sCO_2 [13].

Similar to observations at 750°C [12] and 900°C [28], the mass gains were higher for the specimens of 247, which does not form an Al-rich scale in CO_2 environments but shows significant internal oxidation of Al. An example cross-section from a 247 exposed at 800°C is shown in Figure 6c. For comparison, specimens were included of other Al_2O_3-forming alloys, superalloy X4 and a new wrought Ni-based alumina-forming austenitic alloy, designated NAFA, Table 1. Lower mass gains were observed for these alloys but not significantly different than the best Cr_2O_3-forming alloy 617, see Figure 5. A cross-section of one X4 specimen is shown in Figure 6d. It appeared to have less internal oxidation than the 247 specimen.

DISCUSSION

The alloy 825 specimens performed well at both temperatures which suggests the alloy would be a good candidate for sCO_2 components in the 550°-700°C range. The high Fe content in this alloy did not appear to have a negative effect on sCO_2 compatibility but longer exposures may be needed to evaluate possible C ingress. The initial GDOES results suggest that the Cr-rich scale formed on alloy 825 acts as a C diffusion barrier [24].

Many of the observations appear to be well-explained by composition effects. At 600°C, the best results for an Fe-based alloy were for 709, which contained the highest Cr and Ni contents. The results for CF8C-Plus and 253MA suggest that additions of high levels of Mn (CF8C-Plus) and Si or mischmetal (Ce,La) are not sufficient to prevent Fe-rich nodule formation in sCO_2. While Mn and Si can clearly become incorporated into the scale at 600°C (Figure 3), this may be too low a temperature for reactive elements like Ce and La to show a beneficial effect [29]. The relatively low Ni contents in these two alloys may be an issue in preventing nodule formation.

At 800°C, for the Cr_2O_3-forming alloys, the importance of Al and Ti additions has been shown previously [13,30]. The alloys 617, 825 and 282 with increasing Ti contents show increasing mass gains. Figures 6a and 6b comparing the Cr-rich scales formed on 282 and 825 suggests a thicker external scale on 825 with less internal oxidation than 282. This is likely due to the lower Al content in 825 [30]. For 247, the high Hf content (1.4%) may contribute to the internal oxidation, which was not as significant for X4, with less Hf (0.08%), Table 1. Both alloys have similar Al contents and would be expected to form a continuous Al_2O_3 scale at higher temperatures. Component fabrication might benefit from pre-oxidation to initiate a slow-growing α-Al_2O_3 scale at a higher temperature without CO_2.

Finally, an aspect that has not been addressed yet is the effect of high O_2 and H_2O impurities in the sCO_2 from combustion in the direct-fired Allam cycle [4]. At 750°C, little difference in reaction rates was noted between RG sCO_2 and the low levels (≤50 ppm) of impurities possible in industrial grade sCO_2 [12]. However, the higher impurity levels expected for Allam cycles, compared to indirect-fired or closed cycles,

has been shown to affect reaction rates at 450°-750°C [12,31]. Further work is needed to determine if alloy 825 is affected by high impurity levels. Only limited work has been conducted on the effects of impurities in sCO_2 at elevated temperatures [7,12]. Despite decades of operation, it is not clear from the published literature how the additions (CH_4, H_2O, etc.) in the AGR CO_2 used to prevent oxidation of the graphite moderator in the reactor core may have affected alloy performance in that environment.

SUMMARY

Alloy 825 was compared to a group of advanced austenitic steels at 600°C and Ni-based alloys at 800°C in 300 bar research grade supercritical CO_2. After 1,000 h at 600°C, only the advanced austenitic steel alloy 709 performed as well as 825 under these conditions with both alloys forming thin, protective Cr-rich oxides. Alloy 825 also performed well after 1,000 h in sCO_2 at 800°C compared to a range of Ni-based alloys. Among the Cr_2O_3-forming alloys, the performance of 825 may be explained by its Ti content compared to alloys 617 and 282. High Al content superalloys did not perform significantly better under these conditions at 800°C.

Acknowledgments

The experimental work was conducted by B. Johnston, J. Keiser, T. Lowe, M. Lance, V. Cox and D. Newberry at ORNL. Y.-F. Su and S. Dryepondt provided useful comments on the manuscript. Research sponsored by the U.S. Department of Energy, Office of Fossil Energy and Carbon Management, Crosscutting Technology Program.

References

1. Dostal V, Hejzlar P, Driscoll MJ (2006) The supercritical carbon dioxide power cycle: Comparison to other advanced power cycles. Nucl. Technol. 154(3):283-301.
2. Chen H, Goswami DY, Stefanakos EK (2010) A review of thermodynamic cycles and working fluids for the conversion of low-grade heat. Renewable & Sustainable Energy Rev 14:3059-3067.
3. Iverson BD, Conboy TM, Pasch JJ, Kruizenga AM (2013) Supercritical CO_2 Brayton cycles for solar-thermal energy. Applied Energy 111:957-970.
4. Allam R, Martin S, Forrest B, Fetvedt J, Lu X, Freed D, Brown, Jr. GW, Sasaki T, Itoh M, Manning J (2017) Demonstration of the Allam Cycle: An Update on the Development Status of a High Efficiency Supercritical Carbon Dioxide Power Process Employing Full Carbon Capture. Energy Procedia 114:5948-5966.
5. Olivares RI, Young DJ, Marvig P, Stein W (2015) Alloys SS316 and Hastelloy-C276 in Supercritical CO_2 at High Temperature. Oxid. Met. 84:585–606.
6. Pint BA, Keiser JR, Initial Assessment of Ni-Base Alloy Performance in 0.1 MPa and Supercritical CO_2. JOM 67(11):2615-2620.
7. Mahaffey J, Adam D, Brittan A, Anderson M, Sridharan K (2016) Corrosion of Alloy Haynes 230 in High Temperature Supercritical Carbon Dioxide with Oxygen Impurity Additions. Oxid. Met. 86:567-580.
8. Dheeradhada V, Thatte A, Karadge M, Drobnjak M (2016) Corrosion of Supercritical CO_2 Turbomachinery Components. in Proceedings of the EPRI International Conference on Corrosion in Power Plants, EPRI, Charlotte, NC.
9. Pint BA, Brese RG, Keiser JR (2017) Effect of Pressure on Supercritical CO_2 Compatibility of Structural Alloys at 750°C. Mater. Corros. 68:151-158.
10. Oleksak RP, Tylczak JH, Carney CS, Holcomb GR, Dogan ON (2018) High-Temperature Oxidation of Commercial Alloys in Supercritical CO_2 and Related Power Cycle Environments JOM 70:1527-1534.

11. Pint BA (2018) Performance of Wrought Superalloys in Extreme Environments. in E. Ott et al. (Eds.), *Proceedings of the 9th International Symposium on Superalloy 718 and Derivatives*, TMS, Warrendale, PA, pp.165-178.
12. Pint BA, Lehmusto J, Lance MJ, Keiser JR (2019) The Effect of Pressure and Impurities on Oxidation in Supercritical CO_2. Mater. Corros. 70:1400-1409.
13. Pint BA, Pillai R, Lance MJ, Keiser JR (2020) Effect of Pressure and Thermal Cycling on Long-Term Oxidation in CO_2 and Supercritical CO_2. Oxid. Met. 94:505–526.
14. Feher EG (1968) The Supercritical Thermodynamic Power Cycle. Energy Conversion 8:85-90.
15. Viswanathan R, Shingledecker J, Purgert R (2010) Evaluating Materials Technology for Advanced Ultrasupercritical Coal-Fired Plants. Power 154(8):41-45.
16. Zhao SQ, Xie XS, Smith GD, Patel SJ (2003) Microstructural stability and mechanical properties of a new nickel based superalloy. Mater. Sci. Eng. A 355:96-105.
17. Pike LM (2008) Development of a Fabricable Gamma-Prime (γ′) Strengthened Superalloy. In: Superalloys 2008, R. C. Reed et al. eds, TMS, Warrendale, PA, pp.191-200.
18. Gong Y, Young DJ, Kontis P, Chiu YL, Larsson H, Shin A, Pearson JM, Moody MP, Reed RC (2017) On the breakaway oxidation of Fe9Cr1Mo steel in high pressure CO_2. Acta Mater. 130:361-374.
19. Sarrade S, Férona D, Rouillard F, Perrin S, Robin R, Ruiz JC, Turc HA (2017) Overview on corrosion in supercritical fluids. J. Supercritical Fluids 120:335–344.
20. Shingledecker JP, Pint BA, Sabau AS, Fry AT, Wright IG (2013) Managing Steam-Side Oxidation and Exfoliation in USC Boiler Tubes. Adv. Mater. Processing, 171(1):23-25.
21. Furukawa T, Inagaki Y, Aritomi M (2011) Compatibility of FBR structural materials with supercritical carbon dioxide. Progress in Nuclear Energy 53:1050–1055.
22. McCoy HE (1965) Type 304 Stainless Steel vs Flowing CO_2 at Atmospheric Pressure and 1100-1800°F. Corrosion 21:84-94.
23. Fujii CT, Meussner RA (1967) Carburization of Fe-Cr Alloys During Oxidation in Dry Carbon Dioxide. J. Electrochem. Soc. 114:435-442.
24. Meier GH, Coons WC, R. A. Perkins RA (1982) Corrosion of Iron-, Nickel- and Cobalt-Base Alloys in Atmospheres Containing Carbon and Oxygen. Oxid. Met. 17:235-262.
25. Young DJ, Zhang J, Geers C, Schütze M (2011) Recent advances in understanding metal dusting: A review. Mater. Corros. 62:7-28.
26. Gheno T, Monceau D, Young DJ (2013) Kinetics of breakaway oxidation of Fe-Cr and Fe-Cr-Ni alloys in dry and wet carbon dioxide. Corrosion Science 77:246-256.
27. Pint BA, Pillai R, Keiser JR (2021) Effect of Supercritical CO_2 on Steel Ductility at 450°-650°C. ASME Paper #GT2021-59383, for Turbo Expo 2021, New York, NY.
28. Pint BA, Keiser JR (2022) Exploring Material Solutions for Supercritical CO_2 Applications above 800°C," Oxid. Met. 98:545-559.
29. Pint BA (1996) Experimental Observations in Support of the Dynamic Segregation Theory to Explain the Reactive Element Effect. Oxid. Met. 45:1-37.
30. Lehmusto J, Ievlev AV, Keiser JR, Pint BA (2021) A tracer study on sCO_2 corrosion with multiple oxygen-bearing impurities. Oxid. Met. 96 (2021) 571-587.
31. Pint BA, Lance MJ, Pillai R, Keiser JR (2022) Compatibility of Steels at 450°-650°C in Supercritical CO_2 with O_2 and H_2O Additions. AMPP (formerly NACE) Paper C2022-18018, Houston, TX.

Figure Captions

Figure 1. Specimen mass change after 500 and 1000 h at 600°C in 300 bar sCO_2. The whiskers show one standard deviation of 3-6 specimens exposed at each condition.

Figure 2. Light microscopy of polished cross-sections of specimens after exposure to 300 bar sCO_2 for 1000 h at 600°C (a) 253MA, (b) CF8C-Plus, (c) 709 and (d) 825.

Figure 3. (a) SEM secondary electron image of alloy 709 polished cross-section after 1000 h exposure to 300 bar sCO_2 at 600°C and (b-f) associated EDS maps.

Figure 4. (a) SEM secondary electron image of alloy 825 polished cross-section after 1000 h exposure to 300 bar sCO_2 at 600°C and (b-f) associated EDS maps.

Figure 5. Specimen mass change after 500 and 1000 h at 800°C in 300 bar sCO_2. The whiskers show one standard deviation of 3-6 specimens exposed at each condition.

Figure 6. Light microscopy of polished cross-sections of specimens after exposure to 300 bar sCO_2 for 1000 h at 800°C (a) 282, (b) 825, (c) 247 and (d) X4.

Table 1. Alloy compositions determined by inductively coupled plasma and combustion analyses.

Alloy	Fe	Ni	Cr	Al	Si	Other
316H	69.5	10.0	16.3	0.02	0.46	2.0Mo,0.84Mn,0.3Co,0.3Cu,0.041C,0.04N
CF8C-Plus	61.1	12.8	19.3	0.01	0.57	3.9Mn,0.4Mo,0.5Cu,0.95Nb,0.09C,0.22N
253MA	64.6	11.1	20.6	0.01	1.6	0.69Mn,0.3Mo,0.3Cu,0.17Co,0.03Ce,0.01La, 0.31C,0.15N
709	51.3	25.2	20.1	0.01	0.41	1.49Mo,0.89Mn,0.23Nb,0.02Ti,0.15N,0.06C
825	30.8	39.5	22.7	0.18	0.34	3.0Mo,1.7Cu,0.97Ti,0.55Mn,<5ppmS,0.02C
617	1.2	54.6	22.3	1.0	0.05	11.9Co,8.2Mo,0.4Ti,0.12W,0.04Mn,0.06C
282	0.16	57.1	19.6	1.6	0.04	10.6Co,8.6Mo,2.2Ti,<3ppmS
247	0.07	59.5	8.5	5.7	0.03	9.8Co,9.9W,0.7Mo,3.1Ta,1.0Ti,1.4Hf
X4	0.05	60.8	6.4	5.8	0.02	9.5Co,6.5Ta,6.4W,2.9Re,0.96Ti,0.6Mo,0.08Hf
NAFA*	9.9	Bal.	17.0	4.3		5.5Mo,0.5Ti,0.5W,0.8Mn,0.3C,0.008La
188*	3	22	22		0.35	39Co,14W,1.3Mn,0.03La,0.015B

* nominal values

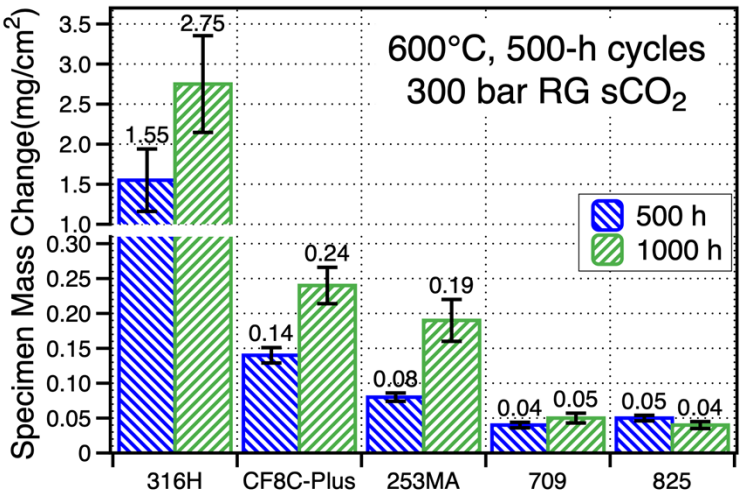

Figure 1. Specimen mass change after 500 and 1000 h at 600°C in 300 bar sCO_2. The whiskers show one standard deviation of 3-6 specimens exposed at each condition.

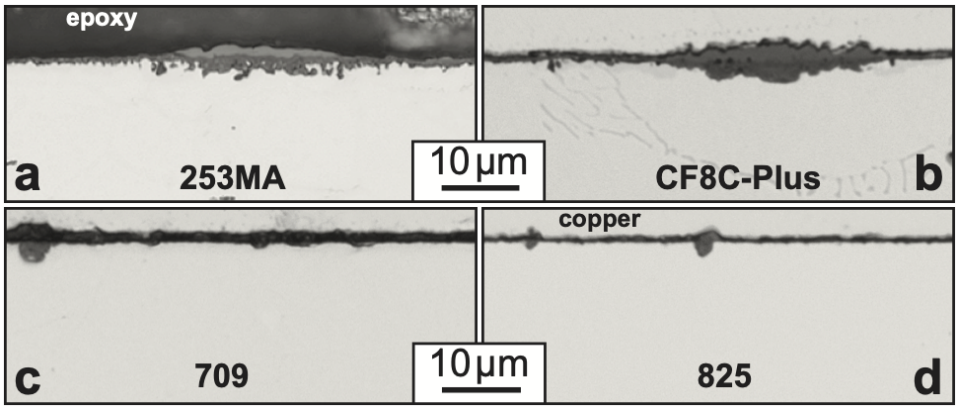

Figure 2. Light microscopy of polished cross-sections of specimens after exposure to 300 bar sCO_2 for 1000 h at 600°C (a) 253MA, (b) CF8C-Plus, (c) 709 and (d) 825.

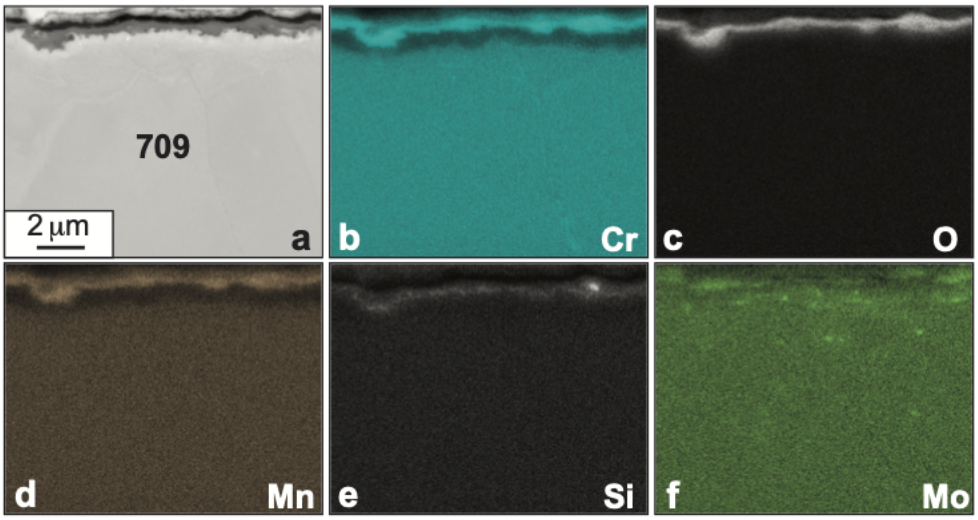

Figure 3. (a) SEM secondary electron image of alloy 709 polished cross-section after 1000 h exposure to 300 bar sCO_2 at 600°C and (b-f) associated EDS maps.

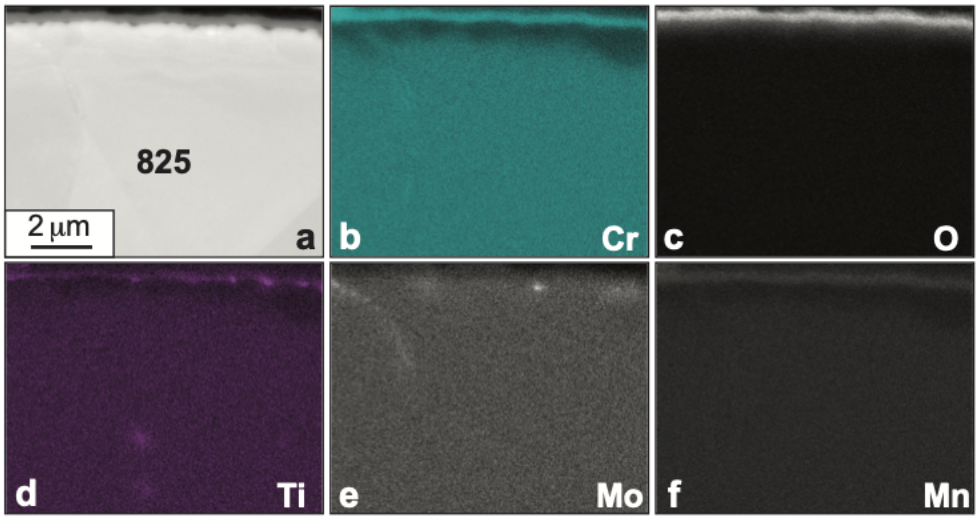

Figure 4. (a) SEM secondary electron image of alloy 825 polished cross-section after 1000 h exposure to 300 bar sCO_2 at 600°C and (b-f) associated EDS maps.

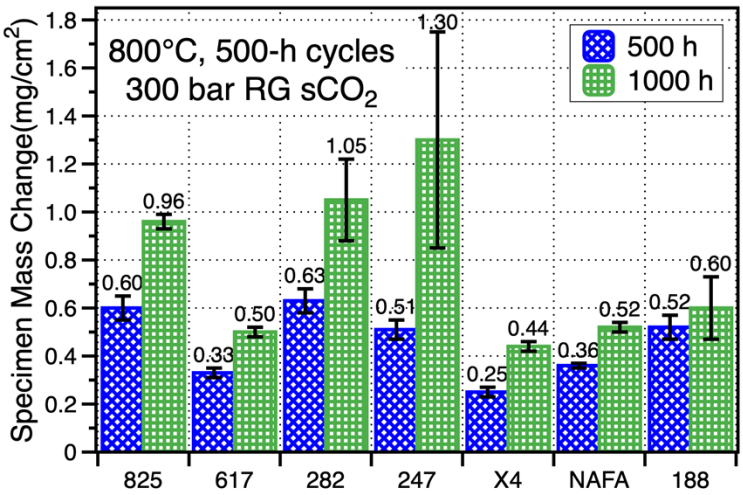

Figure 5. Specimen mass change after 500 and 1000 h at 800°C in 300 bar sCO_2. The whiskers show one standard deviation of 3-6 specimens exposed at each condition.

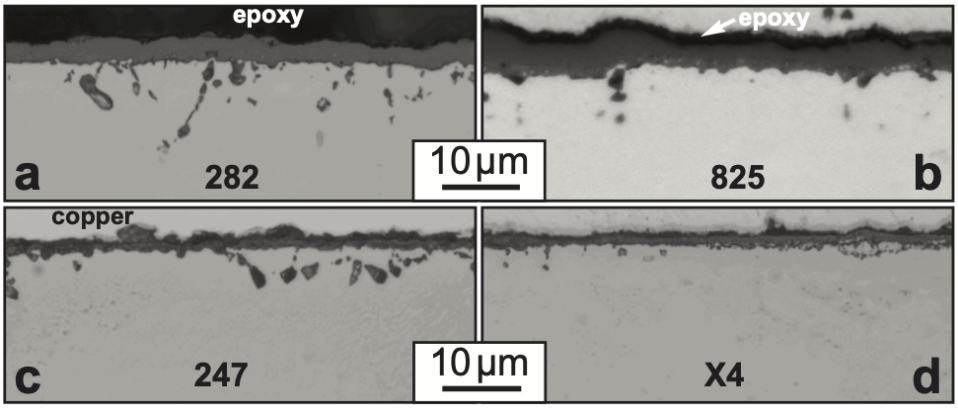

Figure 6. Light microscopy of polished cross-sections of specimens after exposure to 300 bar sCO_2 for 1000 h at 800°C (a) 282, (b) 825, (c) 247 and (d) X4.